



Nitrogen-sulfur co-doped industrial graphene as an efficient peroxyomonosulfate activator: Singlet oxygen-dominated catalytic degradation of organic contaminants



Ping Sun^a, Hui Liu^{a,*}, Mingbao Feng^{b,*}, Li Guo^a, Zhicai Zhai^a, Yingsen Fang^a, Xuesheng Zhang^c, Virender K. Sharma^{b,*}

^a College of Biological, Chemical Sciences and Engineering, Jiaxing University, Zhejiang, Jiaxing 314001, PR China

^b Department of Environmental and Occupational Health, School of Public Health, Texas A&M University, College Station, TX 77843, USA

^c School of Resources and Environmental Engineering, Anhui University, Hefei 230601, PR China

ARTICLE INFO

Keywords:

N-S co-doped industrial graphene (i-rGO-NS)
Nonradical activation
Peroxyomonosulfate (PMS)
Singlet oxygen (${}^1\text{O}_2$)
Parabens

ABSTRACT

This paper presents for the first time the doping of nitrogen (N) and sulfur (S) into industrial reduced graphene oxide (i-rGO) to synthesize the catalyst, named as i-rGO-NS, to activate peroxyomonosulfate (PMS). Co-doping of N and S into the catalyst was investigated by many surface techniques. The i-rGO-NS catalyst had the higher content of graphitic N (~34%) than only N-doped rGO (i.e., i-rGO-N). The i-rGO-NS showed high activation of PMS for catalyzing oxidation of target contaminant, methyl paraben (MP), an endocrine disruptor in water under various conditions (reaction temperature, catalyst loading and PMS dosage). In comparison with the conventional GO and its N-doped or N/S-co-doped composites and classical metal catalysts (e.g., Co_3O_4 and Fe_3O_4), i-rGO-NS has superior effectiveness to activate PMS to degrade contaminants even under the conditions of less dosage of the catalyst (i-rGO-NS) and oxidant (PMS). Results suggest that the N doping, and especially additional S doping were of pivotal in enhancing catalytic performance. Transformation pathways of MP in the i-rGO-NS/PMS system were tentatively proposed that agree with the identified intermediates and frontier electron density calculations. Quenching tests and electron paramagnetic resonance (EPR) studies showed that the singlet oxygen (${}^1\text{O}_2$) was the main reactive oxygen species, revealing that MP degradation follows predominantly the non-radical oxidation pathway. The i-rGO-NS/PMS system not only exhibited considerable removal efficiency of MP in real waters, but also showed the rapid degradation of other pollutants (e.g., UV filter benzophenone-4 (BP-4) and phenol) in water. The newly developed nonradical i-rGO-NS/PMS process is highly effective in decontamination of water.

1. Introduction

Traditional water treatment technology is not adequate to effectively remove the emerging contaminants (ECs) in water, whereas advanced oxidation processes (AOPs) have high efficiency for removing organic pollutants [1]. The sulfate radicals ($\text{SO}_4^{\cdot -}$)-based AOPs have been attracting increasing attentions because of their strong oxidation ability and mineralization efficiency [2,3]. $\text{SO}_4^{\cdot -}$ are generated by activation of peroxyomonosulfate (PMS) and peroxodisulfate (PDS). Activation approaches include ultraviolet light [4], heat [5], transition metals and metal oxides [6–8] and complexes [9], and metal sulfide or phosphide [10,11]. However, the energy requirements or the potential secondary pollutions hindered their applications in the field of water treatment. Therefore, it is highly desirable to develop the efficient,

stable and non-toxic metal-free catalysts in the field of AOPs to activate PMS or PDS to degrade ECs in water.

Nanocarbons (e.g., carbon nanotubes (CNTs) and graphene oxide (GO)) have been applied as the alternative metal-free catalysts to activate PDS and PMS [12–15]. Their catalytic activity can be further enhanced by the heteroatoms doping process [16–18]. Studies on heteroatom-doping of nanocarbon have been mainly focused on their electrocatalytic properties [19–21]. Investigations on their ability to activate PDS and PMS are forthcoming [22]. The application of heteroatom-doped carbon materials in AOPs is attractive because these materials do not require energy supply such as ultraviolet light, high temperature and microwave, and could effectively reduce the formation of secondary pollutants in treatment processes. Another advantage of applying the heteroatom-doped carbon materials is the possible

* Corresponding authors.

E-mail addresses: leolau@163.com (H. Liu), mfeng@tamhsc.edu (M. Feng), vsharma@sph.tamhsc.edu (V.K. Sharma).

involvement of nonradical pathways in degrading ECs. In the PDS/PMS-based-AOPs, $\text{SO}_4^{\cdot-}$ mainly contributes to the degradation of ECs [16,22]. However, only few studies have been performed on applying activation of PDS/PMS using carbon-based materials [23–26]. A non-radical pathway has been suggested in the activation by nanocarbons. More importantly, it remains unclear for the possible contribution of activation pathways by the doped graphene-based catalysts. The study conducted using N/S-co-doped GO showed the radical pathway (i.e., the involvement of $\text{SO}_4^{\cdot-}$ in reaction pathways) [18]. Comparatively, our present study demonstrated the nonradical pathway when industrial reduced graphene oxide (i-rGO) co-doped with N and S was employed as an activator of PMS in degrading the target pollutant, methyl paraben (MP).

Parabens are widely used as the antimicrobial preservatives in food, cosmetics and medicine. They have been extensively detected in indoor air [27], wastewater effluents and sludge [28], environmental water [29,30], and even in human biological samples, such as human urine [31], and human placenta [32]. Parabens have potential endocrine disrupting effects and have received worldwide attention from environmental researchers in the past decades [33]. Incomplete removal of parabens in treatment processes has concerns due to their negative effects to reproductive, neurological and endocrine systems [34–36]. Therefore, it is of utmost importance to develop the highly efficient removal process for treating parabens like MP in water [37,38].

The current paper has the following aims: (i) to demonstrate the successful doping of N and S into i-rGO, (ii) to analyze N and S contents in the prepared catalyst by applying numerous surface techniques. High-level graphitic nitrogen could be doped into the synthesized co-doped catalyst for the first time that has high activation properties, (iii) to investigate the degradation of MP using as prepared activator of PMS under various conditions (temperature and concentrations of catalyst and PMS), (iv) to propose the activation mechanisms and degradation pathways of MP, based on identification of ${}^1\text{O}_2$ and oxidized products and frontier electron density calculations, and (v) to apply the developed system to seek removal of ECs from real water samples.

2. Experimental section

2.1. Materials

Industrial GO (i-GO, > 96%) and industrial rGO (i-rGO, > 96%) were purchased from Leadernano Tech L.L.C, China, and their technical parameters are listed in Table S1. Fe_3O_4 (99.5%, 20 nm), Co_3O_4 (99.5%, 30 nm) and MP were obtained from Macklin Biochemical Co., (Shanghai, China). PMS (> 99%) was acquired from Aladdin (Shanghai, China). Formic acid and methanol (MeOH) of HPLC grades were acquired from Sigma-Aldrich. Ultrapure water (18.2 M Ω cm) was prepared with a water purification system (Millipore, USA).

2.2. Synthesis of doped graphene

N and S co-doped graphene was prepared according to thermal decomposition methods [39]. Typically, after flushing a tube with N_2 for 30 min, a mixture of 0.5 g i-rGO and 0.5 g thiourea was finely grinded. Then the mixture was calcined at 350 °C in a tube furnace. After 1 h, it was cooled to room temperature under N_2 atmosphere, washed with water and ethanol, and then dried under vacuum at 60 °C overnight, and named as i-rGO-NS. Similarly, the samples of i-rGO doped with N or without doping were individually named as i-rGO-N and i-rGO-T, and the doped composites with different atoms at different temperatures were denoted as i-rGO-XYZ-A (XYZ = N, S, P; A = 600, 700, or 800 °C, in which urea and triphenylphosphine were used as N and P sources, respectively). For comparison, i-GO was also doped at 350 °C, and the obtained samples were similarly named as i-GO-N and i-GO-NS.

2.3. Characterization methods

The morphology of the samples was performed on a JEM-2100 F transmission electron microscope (TEM) (JEOL, Japan) and a Quanta400FEG scanning electron microscope (SEM) (FEI, USA). Surface elemental compositions were analyzed using an ESCALAB 250XI X-ray photoelectron spectroscopy (XPS) system (Thermo Fisher Scientific, USA). Nitrogen adsorption-desorption isotherms, specific surface areas, and pore size distributions were measured using a TriStar II 3020 surface area and porosity analyzer (Micromeritics, USA). Raman spectra were collected using a Raman microscope (LabRAM HR Evolution, HORIBA JY, France). The X-ray diffraction (XRD) spectra were measured by a D8-advanced X-ray diffractometer (Bruker, Germany).

2.4. Experimental procedures

The degradation experiments of MP were carried out to evaluate the catalytic performance of the doped rGO catalysts. Specific experimental procedures were performed as follows: 100 mL MP solution (15 mg L $^{-1}$) was taken into conical flask, and a certain amount of PMS was added. The solution was stirred in a constant-temperature water bath. The reaction occurred immediately when a certain amount of catalyst was added. Methanol (0.2 mL) was pre-added in a HPLC vial each time to terminate the reaction at the desired time intervals. 0.8 mL of reaction solution was sampled at certain intervals, followed by filtration through a 0.45 μm Millipore, and the filtrate was in the HPLC vial prior to analysis.

2.5. Analytical methods

The concentration of MP was determined using a LC-20 A HPLC instrument (Shimadzu, Japan), equipped with an Agilent Zorbax SB-C₁₈ column (4.6 \times 250 mm, 5 μm). The mobile phase was a mixture of methanol (A) and 0.3% formic acid solution (B) (60:40 v/v) at a flow rate of 1.0 mL/min. The column temperature was 30 °C and the wavelength of the UV detector was 256 nm.

The samples were extracted using Waters Oasis HLB cartridges (Waters, USA), and then the enriched samples were analyzed by an AB Sciex Qtrap 5600 + MS, coupled with an ESI source and a Shimadzu LC-30 A HPLC. The column was Unitary C₁₈ (1.7 μm , 2.1 mm \times 150 mm); the column temperature was 30 °C; the flow rate was 0.2 mL/min; the injection volume was 2 μL ; and the mobile phase was subjected to a gradient elution procedure using acetonitrile-0.1% formic acid in water. The instrument was set to a negative ion and full scan (50–250 m/z) mode.

For electron paramagnetic resonance (EPR) analysis, an EPR analyzer (Bruker A320, USA) was used to detect the generated reactive oxidative species (ROS). The probing agents used were 5,5-dimethyl-1-pyrroline (DMPO) and 2,2,6,6-tetramethyl-4-piperidone (TEMP). Total organic carbon (TOC) was measured using a Liqui TOC II analyzer (Elmentar, Germany).

2.6. Computational method

To obtain the frontier electron densities (FEDs) of the highest occupied molecular orbital (HOMO) and the lowest unoccupied molecular orbital (LUMO), molecular structure of MP was optimized. Calculations were performed at the B3LYP/6-311 G** level and water solvent model with Gaussian 03 program [40]. Based on the output results, the values of ($\text{FED}_{\text{HOMO}}^2 + \text{FED}_{\text{LUMO}}^2$) and $2\text{FED}_{\text{HOMO}}^2$ were calculated to predict the reaction sites of MP.

Table 1

The chemical composition and distribution of pristine and heteroatom-doped rGO samples.

Samples	C at. %	O at. %	N at. %	S at. %	N distribution at. %				S distribution at. %			
					Pyridinic N	Pyrrolic N	Graphitic N	Oxidized N	S1-I	S1-II	S2-I	S2-II
i-rGO	96.98	2.37	—	0.65	—	—	—	—	45.43	32.22	10.28	12.07
i-rGO-N	95.92	1.57	1.91	0.60	30.10	28.67	25.00	15.93	59.49	40.51	—	—
i-rGO-NS	94.05	1.54	3.31	1.10	32.14	34.12	33.74	—	40.50	38.50	9.63	11.37
i-rGO-NS-recycled	83.81	13.05	2.45	0.69	37.42	28.17	34.41	—	39.90	31.26	23.45	5.39

3. Results and discussion

3.1. Characterization of catalysts

The elemental compositions and chemical states of the doped catalytic samples are shown in **Table 1** and **Fig. 1**, respectively. Generally, four types of N can be included into i-rGO-NS, which include graphitic N, pyridinic N, pyrrolic N, and oxidized N (**Fig. 1A**). The S atom exists in the forms of thiophenic S and oxidized S (**Fig. 1A**). The N content of the co-doped sample (i.e., doping with both N and S or i-rGO-NS) was 3.31 at. % (Atomic %), which was higher than that of only N-doped sample (i-rGO-N, 1.91 at. %) (**Table 1**). This indicates that the N content increased after co-doping procedures, which is possibly due to the synergistic interactions between N and S. Comparatively, the content of S in the i-rGO-NS increased only from 0.65 to 1.10 at. %. It is difficult to incorporate S into the graphene layer due to its larger atomic radius (1.03 Å (S) versus 0.75 Å (C) or 0.71 Å (N)), leading to the relatively low content of S.

The high-resolution N 1 s XPS spectra of i-rGO-N and i-rGO-NS are presented in **Fig. 1B** and C, respectively. Three components of N were found in i-rGO-NS, i.e., pyridinic N at 398.7 eV, pyrrolic N at 399.4 eV, and graphitic N at 400.6 eV. Oxidized N at 404.8 eV was observed in i-rGO-N, but was not found in i-rGO-NS. Moreover, i-rGO-NS had the higher distribution of graphitic N (33.74%) than i-rGO-N, suggesting that the additional S doping might have changed the distribution of N atom in i-rGO-NS. Generally, graphitic N in rGO is formed at high annealing temperature. The rGO-N has 20% graphitic N, prepared by the doping into GO at 700 °C [17]. As known, graphitic N is one of the most active sites in oxygen reduction reaction (ORR) activities and other catalytic reactions [41,42]. The application of i-rGO instead of GO produced more graphitic N, which may enhance the catalytic activation of i-rGO-NS. **Fig. 1E–G** show the high-resolution S 2p XPS spectra of i-rGO, i-rGO-N and i-rGO-NS, respectively. S dopant exists in two forms: thiophenic S (S1, C–S–C, at around 164.1 and 165.4 eV) and oxidized S (S2, C–SOx–C, at around 168.6 and 170.4 eV).

Fig. 2 displays the Raman spectra of i-rGO, i-rGO-N and i-rGO-NS. The characteristic D band (~1340 cm⁻¹) and G band (~1580 cm⁻¹) were found in all samples. Structural disorder is usually estimated by the D/G intensity ratio (I_D/I_G). The i-rGO and the doped samples may have high qualities due to their relatively lower values of I_D/I_G , compared to typical N-doped graphene (1.26) [43] and N/S-co-doped one (1.30) [18], which were prepared by annealing GO with N precursor and with N and S precursors at 350 °C, respectively. However, recent literature reported that the D/G ratio cannot be used to estimate defects in the case of GO and rGO, and thus a new Raman metric ($D'-G_{app}$) was developed [44]. Accordingly, the $D'-G_{app}$ values of i-rGO and i-rGO-NS were calculated as 17.0 and 17.4, respectively, indicating that the co-doping of i-rGO with N and S did not obviously change the degree of reduction. Since their values of $D'-G_{app}$ were smaller than 25, i-rGO and i-rGO-NS were proposed in the form of rGO materials, based on the previous study [44].

The SEM images of i-rGO and i-rGO-NS are shown in **Fig. 3A** and B. The wrinkled sheet and stacked layer morphology can be observed in these two kinds of i-rGOs. The crumpled sheet morphology was further revealed by TEM images. As presented in **Fig. 3A'** and B', two-

dimensional planar structure of i-rGO was retained and the morphology became more crumpled after co-doping with N and S. XRD patterns of the samples showed a characteristic peak at 26° in all samples (**Fig. S1**), and these diffraction peaks had no significant shift, implying that the doping process did not obviously destruct the crystal structure of i-rGO.

The N and S co-doping has an important effect on the pore structure and the surface area of i-rGO materials. The nitrogen adsorption-desorption isotherms and pore size distributions are shown in **Fig. 4**. The type V isotherms of both materials indicate the existence of mesopores in their structures. The SSAs of i-rGO and i-rGO-NS were calculated to be approximately 647.5 ± 11.5 and $576.5 \pm 13.5 \text{ m}^2 \text{ g}^{-1}$, respectively. This suggests the decreased SSA after co-doping with N and S. This may be caused by the merging small pores into larger pores because the mesopore volume at ~2 nm and ~4 nm decreased after doping with N/S atoms.

3.2. Catalytic oxidation of MP

Removal of MP was tested to investigate the activation efficiencies of different catalysts/PMS oxidation systems (**Fig. 5**). The conventional GO and its doped samples as well as the classical metal catalysts (Co_3O_4 and Fe_3O_4) were not effectively able to activate PMS to degrade MP at the tested catalyst dosage and the oxidant usage (**Fig. 5A**). A simple heat treatment of i-rGO did not enhance its activity, but the doping of heteroatoms could do it (**Fig. 5B**). The removal of MP at 30 min were ~5% when only the PMS itself or the activator i-rGO-NS alone was added to the system, indicating that the direct oxidation of PMS and the adsorption of i-rGO-NS were insignificant for removing MP. However, complete elimination of MP was observed in the i-rGO-NS/PMS system. The activations of some other doped i-rGO catalysts with various dopants at different annealing temperatures were also assessed in **Fig. 5C** and D. The performance of N-doped materials was improved when the annealing temperature was increased from 600 to 800 °C, but their performances were all less than the one at 350 °C. This may be because the graphitic N is relatively easier to be formed with the increasing calcination temperature whereas the N content is reduced. Moreover, co-doping with S and ternary doping with S and P at 800 °C could not further improve the catalytic performance of N-doped material. Overall, the prepared i-rGO-NS at 350 °C could effectively activate PMS to remove MP in water, and the activation performance was better than that of the conventional GO- and metal-based catalysts. The reaction conditions for the i-rGO-NS-activated PMS system were further optimized.

The dosage of the catalyst is an important indicator in the wastewater treatment process. The effect of different amounts of i-rGO-NS on the degradation of MP is shown in **Fig. 6A**. The increased dosage of catalyst can significantly improve the degradation of MP. Complete removal of MP was found at 5 min at 40 mg L^{-1} i-rGO-NS. However, the removal of MP was only 60% at a much longer time (i.e., 30 min) at 10 mg L^{-1} i-rGO-NS. The calculated first-order rate constant (k) at 40 mg L^{-1} was $3.5 \times 10^{-1} \text{ min}^{-1}$, which was ~11.7 times higher than that at 10 mg L^{-1} i-rGO-NS ($3.0 \times 10^{-2} \text{ min}^{-1}$). This was expected because the increased amounts of active sites with the increased dosages of catalyst could generate high amounts of ROS in the activation of PMS.

The concentration of PMS also directly affects the production of

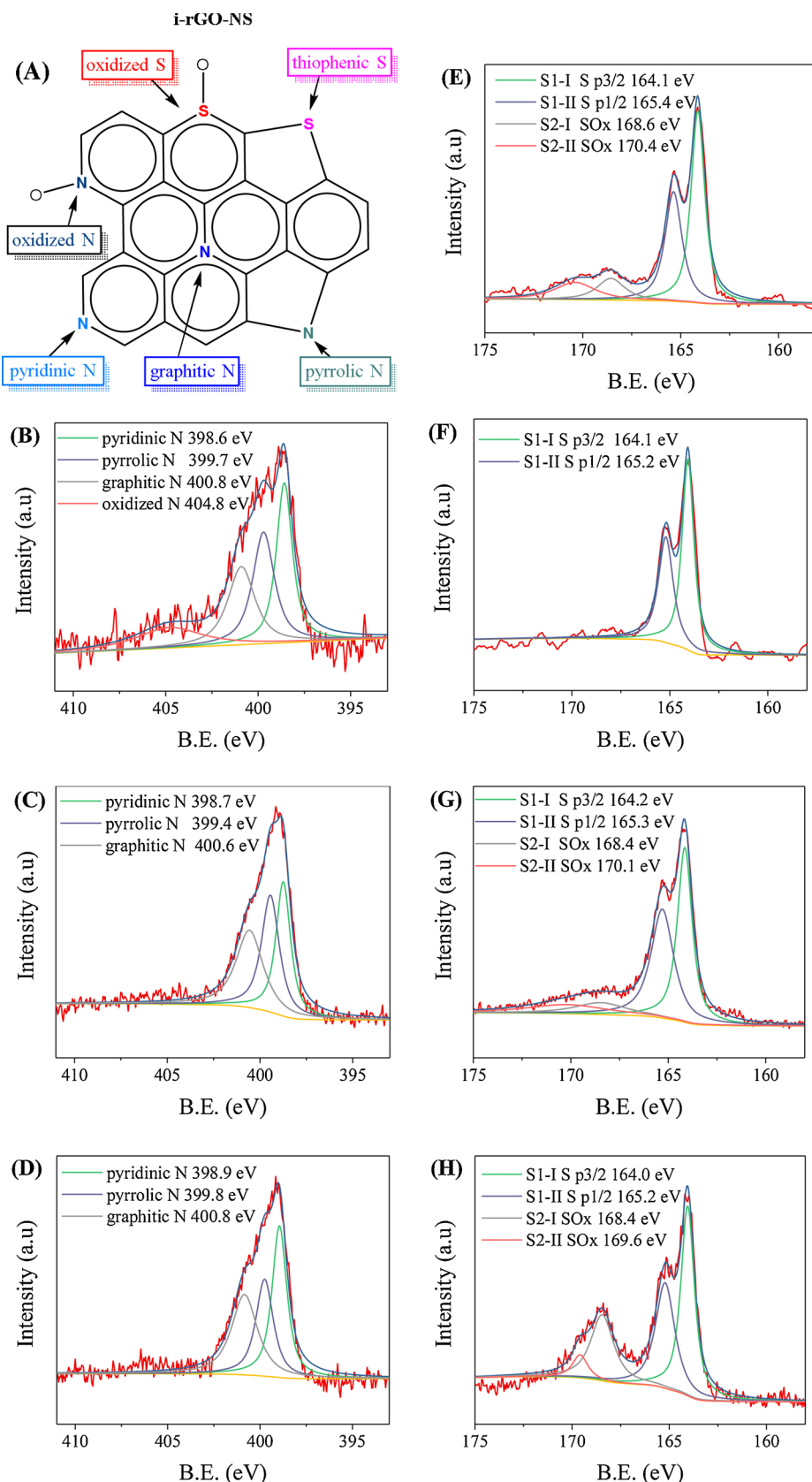


Fig. 1. Schematic illustration of N and S in the carbon lattice (A); N_{1s} spectra of (B) i-rGO-N, (C) i-rGO-NS, (D) i-rGO-NS-recycled; S_{2p} spectra of (E) i-rGO, (F) i-rGO-NS, (G) i-rGO-NS, and (H) i-rGO-NS-recycled.

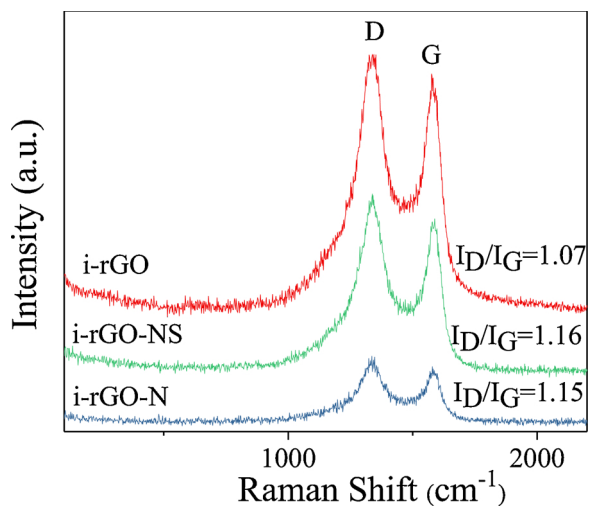


Fig. 2. Raman spectra for i-rGO, i-rGO-N and i-rGO-NS.

ROS in the oxidation system, and therefore the effect of PMS dosage on the removal of MP was investigated. As shown in Fig. 6B, the value of k increased from 1.8×10^{-1} to $2.2 \times 10^{-1} \text{ min}^{-1}$ when the PMS dosage was increased from 0.5 to 1.0 mM. It could be further increased to $5.3 \times 10^{-1} \text{ min}^{-1}$ with an increased dosage of PMS (2.0 mM), whereas a higher dosage of PMS to 10.0 mM only slightly improved the catalytic performance. These findings indicated that the i-rGO-NS is a promising activator of PMS that could even activate a high dosage of PMS (10.0 mM).

In the i-rGO-NS/PMS system, the degradation of MP was also influenced by the temperature. The elevated temperature had a positive effect on the degradation of MP (Fig. 6C). The values of k at 25, 35 and 45 °C were 2.2×10^{-1} , 2.8×10^{-1} and $3.2 \times 10^{-1} \text{ min}^{-1}$, respectively. According to the Arrhenius equation, the activation energy (E_a)

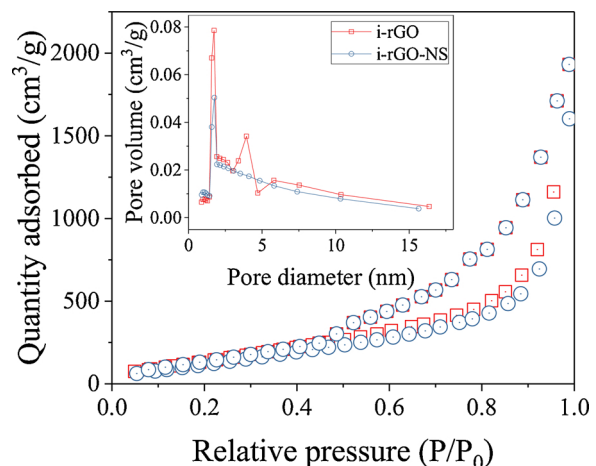


Fig. 4. N_2 sorption isotherms and pore size distributions of i-rGO and i-rGO-NS.

of i-rGO-NS was calculated as 15.0 kJ mol^{-1} in the oxidation system, which is lower than the reported values in other carbon materials/PMS systems (Table S2). This indicates that the catalytic activity of i-rGO-NS was less affected by the reaction temperature. The external energy required for pollutant degradation was lower and the catalyst activity of i-rGO-NS was relatively higher. The decreased activation energy may result from the i-rGO-NS with a larger specific surface area and a higher level of graphitic N, which could easily absorb PMS and pollutants on its surface and therefore facilitated the electron transfer process. This contributed to the high reactivity of i-rGO-NS/PMS system towards the electron-rich moieties of organic compounds (e.g., phenols and MP).

3.3. ROS analysis and activation mechanisms

In order to distinguish the relative contributions of different ROS in

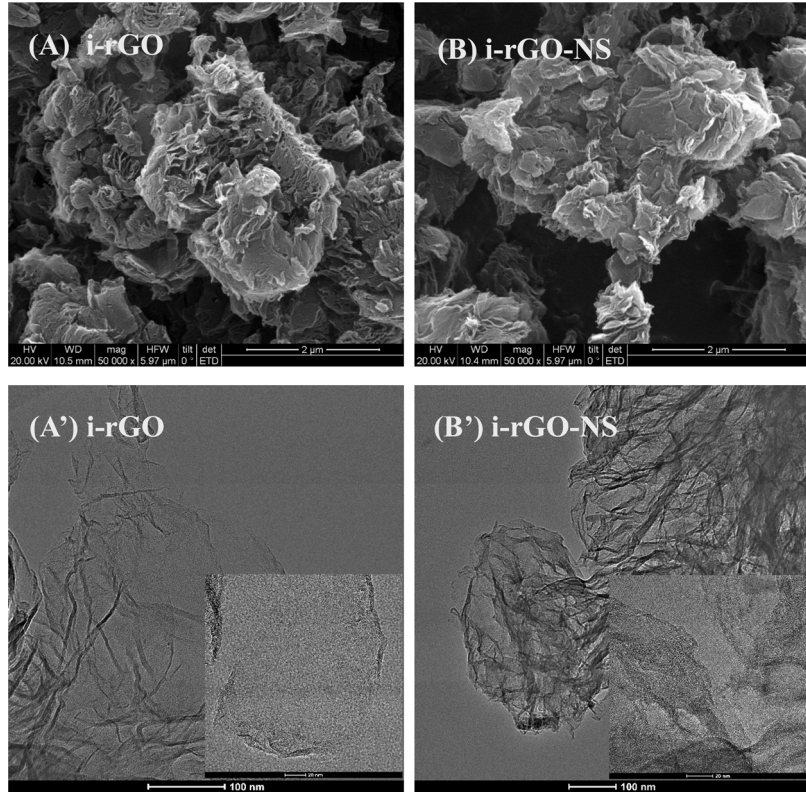


Fig. 3. SEM and TEM images of i-rGO (A, A') and i-rGO-NS (B, B').

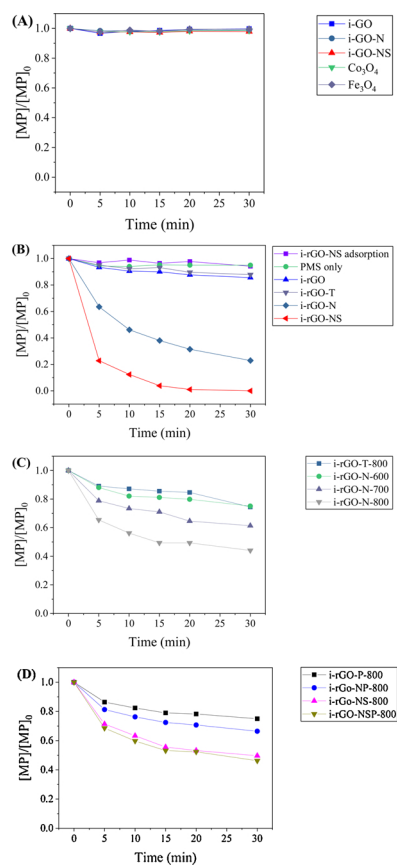


Fig. 5. MP removal efficiencies on various metal or graphene materials. Condition: $[\text{MP}] = 15 \text{ mg L}^{-1}$, $[\text{catalyst}] = 20 \text{ mg L}^{-1}$, $[\text{PMS}] = 307 \text{ mg L}^{-1}$, $T = 25^\circ\text{C}$.

the i-rGO/PMS system, the classical quenching tests were performed during aqueous oxidation of MP. Four commonly used quenchers, ethanol (EtOH), *tert*-butanol (TBA), *p*-benzoquinone (*p*-BQ), and L-histidine (L-His), were used in our study as the scavengers of $\text{SO}_4^{\cdot-}$, $\cdot\text{OH}$, $\text{O}_2^{\cdot-}$, and ${}^1\text{O}_2$, respectively. As shown in Fig. 7, the catalytic degradation rates of MP were not inhibited even using 1000:1 of [EtOH/TBA]:[PMS], which indicated the minor contribution of $\text{SO}_4^{\cdot-}$ and $\cdot\text{OH}$ to MP removal and also the critical role of other reactive species. The degradation of MP was also slightly reduced with the addition of 10 mM *p*-BQ. In contrast, catalytic oxidation of MP was almost completely quenched after adding 10 mM L-His, suggesting the dominated role of ${}^1\text{O}_2$ in efficiently removing MP by the i-rGO-NS/PMS system. We therefore proposed that the major reactive species in this system was ${}^1\text{O}_2$. To further confirm this finding, EPR tests were carried out and the results are presented in Fig. 8. After 5 min, weak DMPO- $\text{SO}_4^{\cdot-}$ and DMPO- $\cdot\text{OH}$ signals were found for PMS activation by i-rGO-NS (Fig. 8A). Additionally, six characteristic peaks of DMPO- OOH were detected, suggesting the existence of $\text{O}_2^{\cdot-}$. More importantly, a strong characteristic triplet signal of TEMP- ${}^1\text{O}_2$ was observed (Fig. 8B), which further confirmed the presence of ${}^1\text{O}_2$ in the i-rGO-NS/PMS oxidation system. In addition, the intensity of TEMP- ${}^1\text{O}_2$ adducts in the i-rGO-NS/PMS oxidation system was higher than those in the i-rGO-N (or i-rGO)/PMS system, indicating that N/S co-doping procedures could facilitate the generation of ${}^1\text{O}_2$. These results were consistent with the radical quenching tests. Hence, the nonradical pathway (involving ${}^1\text{O}_2$) was proposed as the prevailing catalytic reaction. The radical pathway (involving $\text{O}_2^{\cdot-}$, $\text{SO}_4^{\cdot-}$ and $\cdot\text{OH}$) played the minor role.

Generally, pyrrolic N, pyridinic N, graphitic N, and thiophenic S

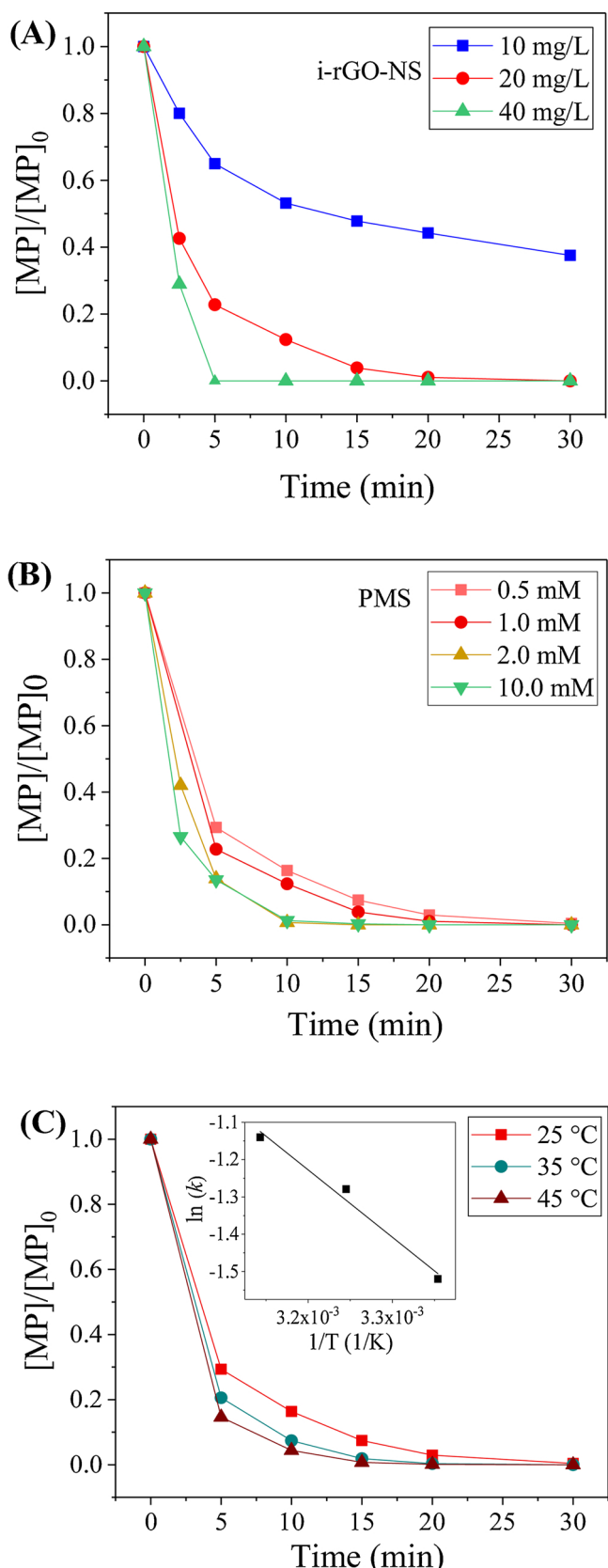


Fig. 6. Influences of (A) i-rGO-NS dose, (B) PMS dose, and (C) reaction temperature. Condition: $[\text{MP}] = 15 \text{ mg L}^{-1}$, $[\text{catalyst}] = 20 \text{ mg L}^{-1}$, $[\text{PMS}] = 307 \text{ mg L}^{-1} = 1 \text{ mM}$, $T = 25^\circ\text{C}$.

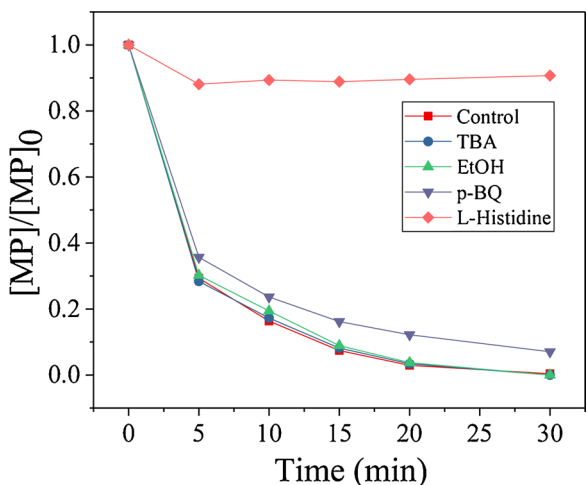


Fig. 7. Influences of different quenchers on PMS oxidation for MP degradation. Condition: $[MP] = 15 \text{ mg L}^{-1}$, $[\text{catalyst}] = 20 \text{ mg L}^{-1}$, $[\text{PMS}] = 307 \text{ mg L}^{-1}$, $T = 25^\circ\text{C}$, $[\text{TBA}] \text{ (or } [\text{EtOH}])/\text{[PMS]} = 1000:1$, $[\text{p-BQ}] = [\text{L-histidine}] = 10 \text{ mM}$.

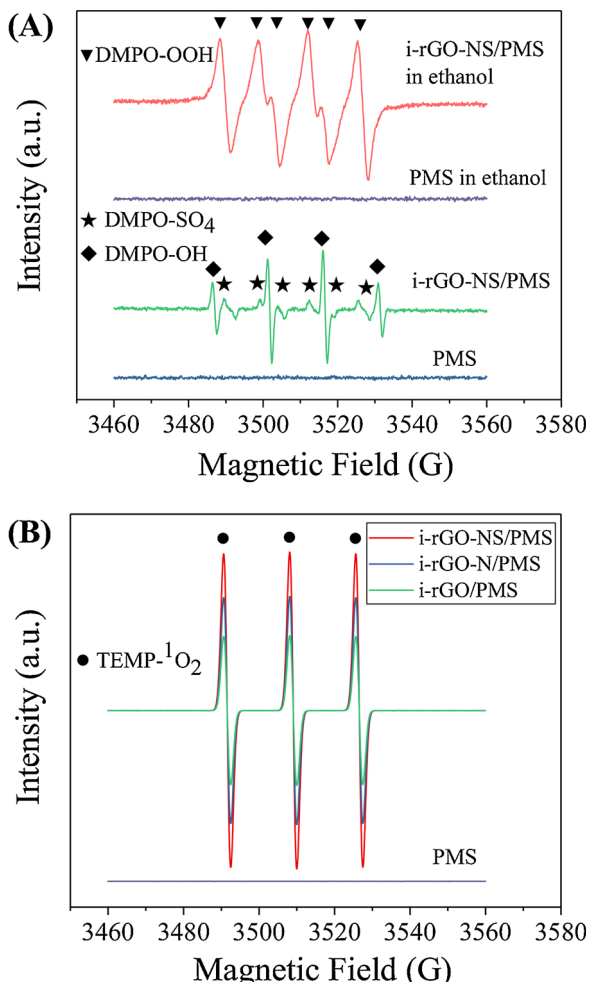
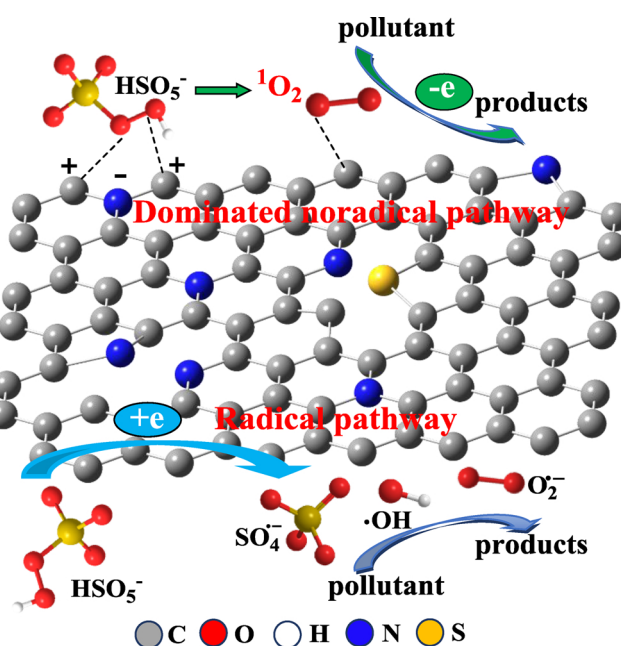


Fig. 8. EPR spectra of (A) DMPO-OH, DMPO-SO₄, DMPO-OOH and (B) TEMP-¹O₂ adduct formed after 5 min in the i-rGO-NS/PMS system. Condition: $[\text{i-rGO-NS}] = 20 \text{ mg L}^{-1}$, $[\text{PMS}] = 307 \text{ mg L}^{-1}$, $T = 25^\circ\text{C}$, $[\text{TEMP}] = 100 \text{ mM}$ and $[\text{DMPO}] = 20 \text{ mM}$.

have some important effects on the catalytic activity of heteroatom-doped carbon catalysts [39]. Pyrrolic and pyridinic N can activate the π electrons of sp^2 C atoms on rGO, which could induce PMS activation to produce $\text{SO}_4^{\cdot-}$ via radical pathway; graphitic N can induce electron transfer from neighboring C. As a result, the positively charged neighboring C would be more susceptible to the nucleophilic addition of PMS to generate ${}^1\text{O}_2$ via nonradical pathway [22]. On the other hand, thiophenic S can also induce the redistributed spin and charge densities and create the positively charged neighboring C [25]. Since the degradation of MP was mainly dominated by the nonradical pathway, graphitic N and thiophenic S may play the critical roles in promoting PMS activation [45,46]. This may be due to the feasibility of more active sites in the nonradical activation of PMS. The strong interactions between the active sites and PMS can oxidize target components directly via extracting electrons from organics without generating free radicals. Additionally, the N-S co-doping procedure presented a synergistic effect on the coupling interactions between N and S [18,39], thus additional S doping in N-doped graphene further increased the catalytic activity. In the past decade, it was believed that $\text{SO}_4^{\cdot-}$ and $\cdot\text{OH}$ play the critical roles in PMS activation by the doped GO-based-catalysts [17,18]. A more recent study also revealed that the sulfacetamide degradation followed predominantly the radical pathway ($\text{SO}_4^{\cdot-}$ as the main ROS) over the nonradical pathway by activation of PMS with N-doped GO through thermal annealing of GO and N precursor [22]. On the contrary, few studies have recently reported the nonradical ${}^1\text{O}_2$ as the dominant ROS in the N-doped-carbons/PMS oxidation system [26,46]. Oh et al. [26] found that the nonradical pathway involving ${}^1\text{O}_2$ generation was the dominant pathway and the graphitic N manifested greatly the catalytic activity during PMS activation by N-doped biomass-derived carbon catalyst. Our results are consistent with this observation. Therefore, it is concluded that a new nonradical oxidation pathway occurred in the i-rGO-NS/PMS system, which is essentially different from the previously proposed radical oxidation pathways during the activation of PMS by graphene-based catalysts.

Generally, ${}^1\text{O}_2$ may be produced through multiple reaction pathways. However, to date, the detailed mechanisms of ${}^1\text{O}_2$ formation on the nanocarbon materials have not been fully elucidated. Based on the characterization of i-rGO-NS and EPR tests, the evolution mechanisms of ${}^1\text{O}_2$ onto i-rGO-NS are proposed in Scheme 1. EPR analysis in



Scheme 1. Mechanism of PMS activation on i-rGO-NS.

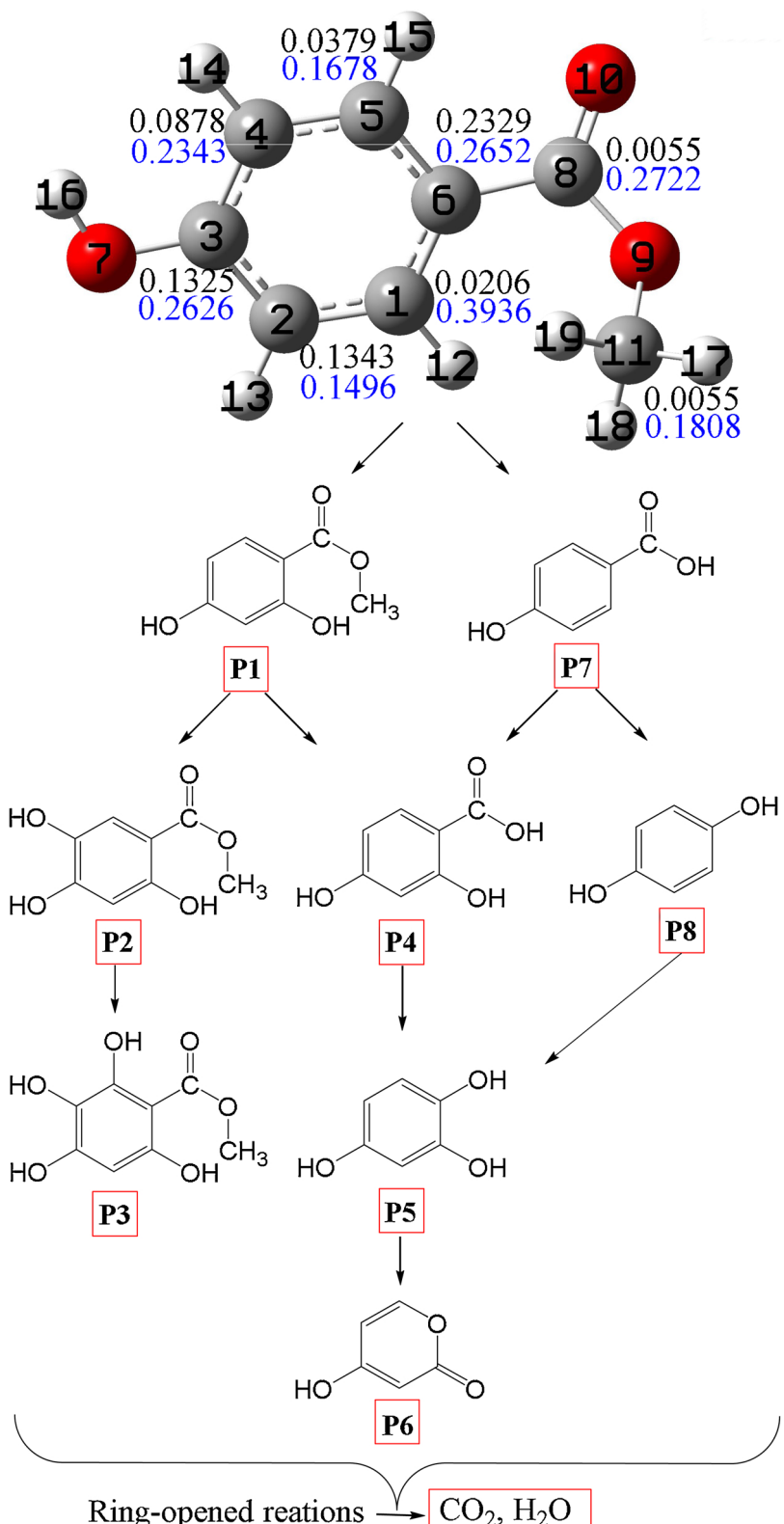
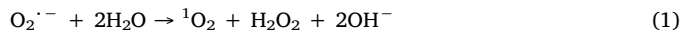


Fig. 9. Proposed reaction pathways for the oxidation of MP by PMS. Blue numbers are the $FED_{HOMO}^2 + FED_{LUMO}^2$ values, and black numbers are the $2FED_{HOMO}^2$ values (For interpretation of the references to colour in this figure legend, the reader is referred to the web version of this article).

conjunction with the quenching experiments suggested the presence of O_2^{--} , which has also been proposed in another study [47]. Basically, direct oxidation or recombination of O_2^{--} may lead to the generation of 1O_2 (Eq. 1). However, the results of quenching tests showed the limited amount of O_2^{--} in our study. In our experiments, 1O_2 can still be

produced, because the degradation of MP slightly decreased when O_2^{--} was quenched by *p*-BQ. These findings indicate that this process might not be the major pathway to generate 1O_2 . On the other hand, it has been suggested that N doping procedure could also induce a nonradical pathway by withdrawing the electrons from neighboring C atoms [26].

In this sense, the positively charged neighboring C atoms can be generated by graphitic N in i-rGO-NS, which facilitated the generation of $^1\text{O}_2$. Therefore, HSO_5^- might be first bonded with these C atoms [45,47], and then the O–O bond in PMS could be activated to generate $^1\text{O}_2$ via the nonradical pathway (Eq. 2), i.e., electron transfer from HSO_5^- to the positively charged C atoms [48].



3.4. MP degradation pathway

The transformation pathways of MP in the i-rGO-NS/PMS system are proposed in Fig. 9, based on eight identified products, of which the MS² information and possible structures are shown in Fig. S2 and Table S2. These intermediates were mainly generated from the oxidation of MP by $^1\text{O}_2$, which could attack the electron-rich groups or carbons by electron transport and/or by formation of endoperoxide intermediates [49]. Accordingly, P1 may be produced by the hydroxylation of MP, which could further occur to sequentially form P2 and P3. Additionally, the demethylation of P1 could produce P4, in which decaboyxilation and further oxidation took place to yield P5 and P6, respectively. On the other hand, similar reactions (e.g., demethylation and hydroxylation) possibly happened to produce P7 and P8.

To validate the initial reaction pathways of MP, the FED calculations of MP were carried out and the results are illustrated in Figs. 9 and S3. According to Fukui's frontier orbit theory [50], the nucleophilic reaction easily occurs in dense places of HOMO, and the electrophilic reaction tends to occur in the dense places of LUMO; the larger the values of $2\text{FED}_{\text{HOMO}}^2$, the more vulnerable the atom is attacked by the oxidant; and the higher values of $\text{FED}_{\text{HOMO}}^2 + \text{FED}_{\text{LUMO}}^2$, the more easily the addition of ROS takes place in these positions. Based on this theory, it can be thus inferred that hydroxylation of MP possibly occurred at the C(1), C(4) and C(5) atoms of the benzene ring due to their higher $\text{FED}_{\text{HOMO}}^2 + \text{FED}_{\text{LUMO}}^2$ values as shown in Fig. 9, leading to the formation of hydroxyl-MP derivatives such as P1, P2 and P3. Similarly, C(6) and C(8) had higher $\text{FED}_{\text{HOMO}}^2 + \text{FED}_{\text{LUMO}}^2$ values, thus P7 and P8 were generated, in which further oxidation took place to yield P4 and P5, respectively. On the other hand, C(6) may be attacked by ROS, which may lead to the opening of the benzene ring, since it possesses the higher $2\text{FED}_{\text{HOMO}}^2$ value. Consequently, P6 and lower organic acids are generated.

3.5. The mineralization and toxicity changes

In order to evaluate the mineralization ability of the system, TOC analysis was conducted, and the results are shown in Fig. S4. After 30 min of oxidation, the TOC value of the reaction solutions of MP reached approximately 70% elimination in the i-rGO-NS/PMS system, suggesting that the i-rGO-NS possessed an excellent catalytic performance for efficiently transforming MP and its organic products to CO_2 and H_2O . The efficient removal of TOC might be ascribed to the non-radical pathway (involving $^1\text{O}_2$ via electron transfer process) and also the radical pathway (involving O_2^\cdot , SO_4^\cdot and $\cdot\text{OH}$). The high removal efficiency (> 50%) of TOC was also reported by $^1\text{O}_2$ -dominated catalytic PMS systems using the heterogeneous catalysts such as N-doped graphene templated by MIL-100(Fe) [51] and N-doped carbon nanotubes frameworks [52].

Based on the globally harmonized system of classification and labelling of chemicals [53], hazard chemicals can be classified and labelled as 'very toxic' ($\text{LC}_{50} \leq 1 \text{ mg/L}$), 'toxic' ($1 < \text{LC}_{50} \leq 10 \text{ mg/L}$), 'harmful' ($10 < \text{LC}_{50} \leq 100 \text{ mg/L}$), or 'not harmful' ($\text{LC}_{50} > 100 \text{ mg/L}$), respectively. To assess the change of toxicity, the values of LC_{50} for MP and its intermediates were predicted by a Toxicity Estimation Software Tool [54], and then were classified (Table S3). Except P2 and

P3, almost all degradation products were less toxic to *Fathead minnow* and *Daphnia magna* than the parent compound (MP) and can be classified as 'harmful' or 'not harmful'. In conclusion, MP can mainly be converted into low or non-harmful products in this new oxidation system. The i-rGO-NS/PMS system can not only rapidly degrade MP, but also convert it into CO_2 and H_2O and other harmless organic substances.

3.6. Effect of the water matrix

Generally, NO_3^- , SO_4^{2-} , Cl^- , and various organic components are present in real waters, and their existence may affect the degradation of MP in the i-rGO-NS/PMS system. Therefore, it is necessary to investigate the effects of these anions and humic acid (HA) on the removal efficiency of MP in water. As shown in Fig. S5, almost complete elimination of MP can still be obtained after adding different anions (5 mM) to the solution. This suggests that the presence of anions (5 mM) in water had little effect on the removal efficiency compared with the control experiment. In the use of HA (5–20 mg L⁻¹), the removal efficiency of MP was decreased. The corresponding values of k were 18.0×10^{-2} , 9.7×10^{-2} and $3.7 \times 10^{-2} \text{ min}^{-1}$ at the levels of HA as 5.0, 10.0 and 20.0 mg L⁻¹, respectively. These results showed that HA competed with the target pollutant to react with the reactive species produced in this catalytic oxidation system. The competitiveness could be possibly increased with the increasing dosages of HA, resulting in the decreasing removal rate of MP.

Furthermore, the real water environment is variable. In order to further evaluate the practical efficiency of i-rGO-NS-activated PMS system to remove MP, tap water and filtered surface water were spiked with MP for the removal experiments. The water quality parameters of these water samples are given in Table S4, and the experimental results are presented in Fig. S6. Removal of MP up to 90% could be seen within 30 min of oxidation, and complete removal was found when the double dosage of i-rGO-NS was used. This indicates that i-rGO-NS-activated PMS system is also effective in removing MP from real water samples.

3.7. Comparison with some other reported catalysts

In our previous study, we have prepared a novel NS-co-doped CNT by using a carboxylated CNT as carbon source, and this catalyst can remarkably activate PMS to effectively degrade BP-4 [39]. Duan et al. [18] also prepared a NS-co-doped GO and then used it as the PMS activator to remove phenol in water. Therefore, in this study, to further test the versatility of the i-rGO-NS/PMS system, BP-4 and phenol were also chosen as the target pollutants for comparison, and the detailed conditions and the results of their degradation are shown in Table S5 and Fig. S7, respectively. The i-rGO-NS/PMS oxidation system can completely remove BP-4 or phenol within the same time or even less time. Significantly, it only needs much less dosages of catalyst and PMS, suggesting the i-rGO-NS as a superior catalyst for remediating pollutants.

3.8. Stability of i-rGO-NS

To assess the stability and reusability of i-rGO-NS, a specific experiment was conducted as follows: i-rGO-NS was added to the mixed solution of 15 mg L⁻¹ MP and 1 mM PMS. The catalyst was separated after 30 min of reaction, then washed by water and ethanol in an ultrasound device and dried at 60 °C. The treated catalyst was then added to a freshly mixed solution for the second degradation experiment (30 min), and the results are shown in Fig. S8. Approximately 80% of MP could be eliminated after 60 min in the second run. The recycled i-rGO-NS catalyst was also characterized. No obvious changes were noticed in crystal structures and the wrinkled sheets after the first run based on the analysis of XRD spectra (Fig. S1) and SEM/TEM images (Fig. S9). However, XPS showed a decrease in level of N to 2.45 at. %

and an increase of O content to 13.05 at. % in the recycled i-rGO-NS (Table 1). It may thus be deduced that the loss of dopants and the surface-active sites (due to the adsorption of intermediates) might lead to the deactivation of the catalyst. Generally, the used catalysts can be recovered by heat treatment again [22,55]. In this study, the catalyst loading was relatively lower than any other reported nanocatalysts used in the similar degradation system. Therefore, the removal efficiency can be significantly improved (i.e., complete elimination of MP after 30 min of catalytic oxidation) by increasing the dosage of the catalyst in the later reuse experiment, as shown in Fig. S8.

4. Conclusions

Using industrial rGO instead of common GO as a carbon source, N and S co-doped graphene material (i-rGO-NS) was synthesized in this study. The i-rGO-NS was demonstrated as a more efficient activator of PMS for the catalytic degradation of MP than conventional doped graphene materials and classical metal catalysts. The characterization results indicated that the synergistic effect of N and S co-doping process was responsible for the enhanced catalytic performance. The degradation reaction follows the pseudo first-order kinetic model, and the degradation rates of MP were influenced by different experimental factors (e.g., PMS concentration, catalyst dosage and reaction temperature). The degradation pathways of MP in the i-rGO-NS/PMS oxidation system were proposed, which agreed with eight identified intermediates. The main reactive species was proposed as $^1\text{O}_2$, which can trigger the nonradical oxidation of MP for its efficient elimination in water. Overall, these findings could contribute to the development of heteroatoms doped industrial graphene-based nanocatalysts and also the potential applications of i-rGO-NS as a novel activator of PMS in AOPs for water depollution.

Acknowledgments

The authors acknowledge financial supported from the National Natural Science Foundation of China (No. 21607058 and 21607001), the Zhejiang Provincial Department of Education General Research Project (No. Y201840526) and the Jiaxing Clean Production Innovation Team of Leather and Textile Dyeing & Finishing. We wish to thank anonymous reviewers for their comments, which improve the paper greatly.

Appendix A. Supplementary data

Supplementary material related to this article can be found, in the online version, at doi:<https://doi.org/10.1016/j.apcatb.2019.03.085>.

References

- [1] U. von Gunten, Oxidation processes in water treatment: are we on track? *Environ. Sci. Technol.* 52 (9) (2018) 5062–5075.
- [2] Y.Y. Ahn, H. Bae, H.I. Kim, S.H. Kim, J.H. Kim, S.G. Lee, J. Lee, Surface-loaded metal nanoparticles for peroxymonosulfate activation: efficiency and mechanism reconnaissance, *Appl. Catal. B: Environ.* 241 (2019) 561–569.
- [3] Y. Zhou, X.L. Wang, C.Y. Zhu, D.D. Dionysiou, G.C. Zhao, G.D. Fang, D.M. Zhou, New insight into the mechanism of peroxymonosulfate activation by sulfur-containing minerals: role of sulfur conversion in sulfate radical generation, *Water Res.* 142 (2018) 208–216.
- [4] J.S. Ye, P.L. Zhou, Y. Chen, H.S. Ou, J. Liu, C.S. Li, Q.S. Li, Degradation of 1H-benzotriazole using ultraviolet activating persulfate: mechanisms, products and toxicological analysis, *Chem. Eng. J.* 334 (2018) 1493–1501.
- [5] Y.F. Ji, Y.Y. Shi, W. Dong, X. Wen, M.D. Jiang, J.H. Lu, Thermo-activated persulfate oxidation system for tetracycline antibiotics degradation in aqueous solution, *Chem. Eng. J.* 298 (2016) 225–233.
- [6] X.G. Duan, C. Su, J. Miao, Y.J. Zhong, Z.P. Shao, S.B. Wang, H.Q. Sun, Insights into perovskite-catalyzed peroxymonosulfate activation: maneuverable cobalt sites for promoted evolution of sulfate radicals, *Appl. Catal. B: Environ.* 220 (2018) 626–634.
- [7] M.B. Feng, R.J. Qu, X.L. Zhang, P. Sun, Y.X. Sui, L.S. Wang, Z.Y. Wang, Degradation of flumequine in aqueous solution by persulfate activated with common methods and polyhydroquinone-coated magnetite/multi-walled carbon nanotubes catalysts, *Water Res.* 85 (2015) 1–10.
- [8] M.B. Feng, L. Cizmas, Z.Y. Wang, V.K. Sharma, Synergistic effect of aqueous removal of fluoroquinolones by a combined use of peroxymonosulfate and ferrate(VI), *Chemosphere* 177 (2017) 144–148.
- [9] R.B. Li, M.X. Cai, Z.J. Xie, Q.X. Zhang, Y.Q. Zeng, H.J. Liu, G.P. Liu, W.Y. Lv, Construction of heterostructured CuFe₂O₄/g-C₃N₄ nanocomposite as an efficient visible light photocatalyst with peroxydisulfate for the organic oxidation, *Appl. Catal. B: Environ.* 244 (2019) 974–982.
- [10] H.D. Xu, D. Wang, J. Ma, T. Zhang, X.H. Lu, Z.Q. Chen, A superior active and stable spinel sulfide for catalytic peroxymonosulfate oxidation of bisphenol S, *Appl. Catal. B: Environ.* 238 (2018) 557–567.
- [11] C. Alexopoulou, A. Petala, Z. Frontistis, C. Drivas, S. Kennou, D.I. Kondarides, D. Mantzavinos, Copper phosphide and persulfate salt: a novel catalytic system for the degradation of aqueous phase micro-contaminants, *Appl. Catal. B: Environ.* 244 (2019) 178–187.
- [12] S. Indrawirawan, H.Q. Sun, X.G. Duan, S.B. Wang, Nanocarbons in different structural dimensions (0–3D) for phenol adsorption and metal-free catalytic oxidation, *Appl. Catal. B: Environ.* 179 (2015) 352–362.
- [13] L. Bekris, Z. Frontistis, G. Trakakis, L. Sygellou, C. Galiotis, D. Mantzavinos, Graphene: a new activator of sodium persulfate for the advanced oxidation of parabens in water, *Water Res.* 126 (2017) 111–121.
- [14] C.T. Guan, J. Jiang, C.W. Luo, S.Y. Pang, Y. Yang, Z. Wang, J. Ma, J. Yu, X. Zhao, Oxidation of bromophenols by carbon nanotube activated peroxymonosulfate (PMS) and formation of brominated products: comparison to peroxydisulfate (PDS), *Chem. Eng. J.* 337 (2018) 40–50.
- [15] E.T. Yun, H.Y. Yoo, H. Bae, H. Kim, J. Lee, Exploring the role of persulfate in the activation process: radical precursor versus electron acceptor, *Environ. Sci. Technol.* 51 (2017) 10090–10099.
- [16] H.Q. Sun, C. Kwan, A. Suvorova, H.M. Ang, M.O. Tadé, S.B. Wang, Catalytic oxidation of organic pollutants on pristine and surface nitrogen-modified carbon nanotubes with sulfate radicals, *Appl. Catal. B: Environ.* 154–155 (2014) 134–141.
- [17] X.G. Duan, Z.M. Ao, H.Q. Sun, S. Indrawirawan, Y.X. Wang, J. Kang, F.L. Liang, Z.H. Zhu, S.B. Wang, Nitrogen-doped graphene for generation and evolution of reactive radicals by metal-free catalysis, *ACS Appl. Mater. Interfaces* 7 (2015) 4169–4178.
- [18] X.G. Duan, K. O'Donnell, H.Q. Sun, Y.X. Wang, S.B. Wang, Sulfur and nitrogen co-doped graphene for metal-free catalytic oxidation reactions, *Small* 11 (2015) 3036–3044.
- [19] L.L. Hu, F. Peng, D.H. Xia, H.J.W. He, C. He, Z.K. Fang, J.L. Yang, S.H. Tian, V.K. Sharma, D. Shu, Carbohydrates-derived nitrogen-doped hierarchical porous carbon for ultrasensitive detection of 4-nitrophenol, *ACS Sustain. Chem. Eng.* 6 (2018) 17391–17401.
- [20] M. Kaur, M. Kaur, V.K. Sharma, Nitrogen-doped graphene and graphene quantum dots: a review on synthesis and applications in energy, sensors and environment, *Adv. Colloid Interfac.* 259 (2018) 44–64.
- [21] V.K. Sharma, T.J. McDonald, H. Kim, V.K. Garg, Magnetic graphene-carbon nanotube iron nanocomposites as adsorbents and antibacterial agents for water purification, *Adv. Colloid Interfac.* 225 (2015) 229–240.
- [22] X. Chen, W.D. Oh, Z.T. Hu, Y.M. Sun, R.D. Webster, S.Z. Li, T.T. Lim, Enhancing sulfacetamide degradation by peroxymonosulfate activation with N-doped graphene produced through delicately-controlled nitrogen functionalization via tweaking thermal annealing processes, *Appl. Catal. B: Environ.* 225 (2018) 243–257.
- [23] X.G. Duan, H.Q. Sun, Z.P. Shao, S.B. Wang, Nonradical reactions in environmental remediation processes uncertainty and challenges, *Appl. Catal. B: Environ.* 224 (2018) 973–982.
- [24] P. Liang, C. Zhang, X.G. Duan, H.Q. Sun, S.M. Liu, M.O. Tadea, S.B. Wang, An insight into metal organic framework derived N-doped graphene for the oxidative degradation of persistent contaminants: formation mechanism and generation of singlet oxygen from peroxymonosulfate, *Environ. Sci. Nano* 4 (2017) 315–324.
- [25] Y.P. Guo, Z.Q. Zeng, Y.C. Zhu, Z.G. Huang, Y. Cui, J.Y. Yang, Catalytic oxidation of aqueous organic contaminants by persulfate activated with sulfur-doped hierarchically porous carbon derived from thiophene, *Appl. Catal. B: Environ.* 220 (2018) 635–644.
- [26] W.-D. Oh, G. Lisak, R.D. Webster, Y.-N. Liang, A. Veksha, A. Giannis, J.G.S. Moo, J.-W. Lim, T.-T. Lim, Insights into the thermolytic transformation of lignocellulosic biomass waste to redox-active carbocatalyst: durability of surface active sites, *Appl. Catal. B: Environ.* 233 (2018) 120–129.
- [27] J. Chen, E.M. Hartmann, J. Kline, K. Van Den Wymelenberg, R.U. Halden, Assessment of human exposure to triclocarban, tricosan and five parabens in U.S. Indoor dust using dispersive solid phase extraction followed by liquid chromatography tandem mass spectrometry, *J. Hazard. Mater.* 360 (2018) 623–630.
- [28] W.L. Ma, X. Zhao, Z.F. Zhang, T.F. Xu, F.J. Zhu, Y.F. Li, Concentrations and fate of parabens and their metabolites in two typical wastewater treatment plants in northeastern China, *Sci. Total Environ.* 644 (2018) 754–761.
- [29] M. Česen, M. Ahel, S. Terzić, D.J. Heath, E. Heath, The occurrence of contaminants of emerging concern in Slovenian and Croatian wastewaters and receiving Sava river, *Sci. Total Environ.* 650 (2019) 2446–2453.
- [30] X.Q. Ma, Y.J. Wan, M.Y. Wu, Y. Xu, Q. Xu, Z.Y. He, W. Xia, Occurrence of benzophenones, parabens and triclosan in the Yangtze River of China, and the implications for human exposure, *Chemosphere* 213 (2018) 517–525.
- [31] M. Honda, M. Robinson, K. Kannan, Parabens in human urine from several Asian countries, Greece, and the United States, *Chemosphere* 201 (2018) 13–19.
- [32] J. Valle-Sistac, D. Molins-Delgado, M. Diaz, L. Ibáñez, D. Barceló, M.S. Diaz-Cruz, Determination of parabens and benzophenone-type UV filters in human placenta. First description of the existence of benzyl paraben and benzophenone-4, *Environ.*

- Int. 88 (2016) 243–249.
- [33] K. Nowak, W. Ratajczak-Wrona, M. Górska, E. Jabłońska, Parabens and their effects on the endocrine system, *Mol. Cell. Endocrinol.* 474 (2018) 238–251.
- [34] J. Lu, H.P. Li, Y. Tu, Z.G. Yang, Biodegradation of four selected parabens with aerobic activated sludge and their transesterification product, *Ecotox. Environ. Saf.* 156 (2018) 48–55.
- [35] D.C. Silva, L. Serrano, T.M.A. Oliveira, A.S. Mansano, E.A. Almeida, E.M. Vieira, Effects of parabens on antioxidant system and oxidative damages in Nile tilapia (*Oreochromis niloticus*) ewcotox, *Environ. Saf.* 162 (2018) 85–91.
- [36] A.Z. Pollack, S.L. Mumford, J.R. Krall, A.E. Carmichael, L.A. Sjaarda, N.J. Perkins, K. Kannan, E.F. Schisterman, Exposure to bisphenol A, chlorophenols, benzophenones, and parabens in relation to reproductive hormones in healthy women: a chemical mixture approach, *Environ. Int.* 120 (2018) 137–144.
- [37] Y.Q. Chen, P.Y. Deng, P.C. Xie, R. Shang, Z.P. Wang, S.L. Wang, Heat-activated persulfate oxidation of methyl- and ethyl-parabens: effect, kinetics, and mechanism, *Chemosphere* 168 (2017) 1628–1636.
- [38] J.F. Gomes, A. Lopes, M. Gmurek, R.M. Quinta-Ferreira, R.C. Martins, Study of the influence of the matrix characteristics over the photocatalytic ozonation of parabens using Ag-TiO₂, *Sci. Total Environ.* 646 (2019) 1468–1477.
- [39] H. Liu, P. Sun, M.B. Feng, H.X. Liu, S.G. Yang, L.S. Wang, Z.Y. Wang, Nitrogen and sulfur co-doped CNT-COOH as an efficient metal-free catalyst for the degradation of UV filter BP-4 based on sulfate radicals, *Appl. Catal. B: Environ.* 187 (2016) 1–10.
- [40] M.J. Frisch, G.W. Trucks, H.B. Schlegel, G.E. Scuseria, M.A. Robb, J.R. Cheeseman, J.A. Montgomery Jr., T. Vreven, K.N. Kudin, J.C. Burant, J.M. Millam, S.S. Iyengar, J. Tomasi, V. Barone, B. Mennucci, M. Cossi, G. Scalmani, N. Rega, G.A. Petersson, H. Nakatsuji, M. Hada, M. Ehara, K. Toyota, R. Fukuda, J. Hasegawa, M. Ishida, T. Nakajima, Y. Honda, O. Kitao, H. Nakai, M. Klene, X. Li, J.E. Knox, H.P. Hratchian, J.B. Cross, V. Bakken, C. Adamo, J. Jaramillo, R. Gomperts, R.E. Stratmann, O. Yazyev, A.J. Austin, R. Cammi, C. Pomelli, J.W. Ochterski, P.Y. Ayala, K. Morokuma, G.A. Voth, P. Salvador, J.J. Dannenberg, V.G. Zakrzewski, S. Dapprich, A.D. Daniels, M.C. Strain, O. Farkas, D.K. Malick, A.D. Rabuck, K. Raghavachari, J.B. Foresman, J.V. Ortiz, Q. Cui, A.G. Baboul, S. Clifford, J. Cioslowski, B.B. Stefanov, G. Liu, A. Liashenko, P. Piskorz, I. Komaromi, R.L. Martin, D.J. Fox, T. Keith, M.A. Al-Laham, C.Y. Peng, A. Nanayakkara, M. Challacombe, P.M.W. Gill, B. Johnson, W. Chen, M.W. Wong, C. Gonzalez, J.A. Pople, Gaussian 03, Revision E.01, Gaussian, Inc, Wallingford CT, 2004.
- [41] X.Y. Lu, D. Wang, L.P. Ge, L.H. Xiao, H.Y. Zhang, L.L. Liu, J.Q. Zhang, M.Z. An, P.X. Yang, Enriched graphitic N in nitrogen-doped graphene as a superior metal-free electrocatalyst for the oxygen reduction reaction, *New J. Chem.* 42 (2018) 19665–19670.
- [42] Y.H. Su, H.L. Jiang, Y.H. Zhu, X.L. Yang, J.H. Shen, W.J. Zou, J.D. Chen, C.Z. Li, Enriched graphitic N-doped carbon-supported Fe₃O₄ nanoparticles as efficient electrocatalysts for oxygen reduction reaction, *J. Mater. Chem. A* 2 (2014) 7281–7287.
- [43] S. Indrawiran, H.Q. Sun, X.G. Duan, S.B. Wang, Low temperature combustion synthesis of nitrogen-doped graphene for metal-free catalytic oxidation, *J. Mater. Chem. A* 3 (2015) 3432–3440.
- [44] A.A.K. King, B.R. Davies, N. Noorbehesht, P. Newman, T.L. Church, A.T. Harris, J.M. Razal, A.I. Minett, A new Raman metric for the characterisation of graphene oxide and its derivatives, *Sci. Rep.* 6 (2016) 1–6.
- [45] X.G. Duan, H.Q. Sun, Y.X. Wang, J. Kang, S.B. Wang, N-doping-induced nonradical reaction on single-walled carbon nanotubes for catalytic phenol oxidation, *ACS Catal.* 5 (2015) 553–559.
- [46] H.W. Sun, X.X. Peng, S.P. Zhang, S.W. Liu, Y. Xiong, S.H. Tian, J.Y. Fang, Activation of peroxyxonosulfate by nitrogen-functionalized sludge carbon for efficient degradation of organic pollutants in water, *Bioresour. Technol.* 241 (2017) 244–251.
- [47] S.S. Zhu, X.J. Li, J. Kang, X.G. Duan, S.B. Wang, Persulfate activation on crystallographic manganese oxides: mechanism of singlet oxygen evolution for nonradical selective degradation of aqueous contaminants, *Environ. Sci. Technol.* 53 (2019) 307–315.
- [48] Y.W. Gao, Y. Zhu, L. Lyu, Q.Y. Zeng, X.C. Xing, C. Hu, Electronic structure modulation of graphitic carbon nitride by oxygen doping for enhanced catalytic degradation of organic pollutants through peroxyxonosulfate activation, *Environ. Sci. Technol.* 52 (2018) 14371–14380.
- [49] Y. Zhou, J. Jiang, Y. Gao, S.-Y. Pang, Y. Yang, J. Ma, J. Gu, J. Li, Z. Wang, L.-H. Wang, L.-P. Yuan, Y. Yang, Activation of peroxyxonosulfate by phenols: important role of quinone intermediates and involvement of singlet oxygen, *Water Res.* 125 (2017) 209–218.
- [50] K. Fukui, T. Yonezawa, H. Shingu, A molecular orbital theory of reactivity in aromatic hydrocarbons, *J. Chem. Phys.* 20 (1952) 722.
- [51] P. Liang, C. Zhang, X.G. Duan, H.Q. Sun, S.M. Liu, M.O. Tade, S.B. Wang, N-doped graphene from metal–organic frameworks for catalytic oxidation of p-hydroxybenzoic acid: N-Functionality and mechanism, *ACS Sustain. Chem. Eng.* 5 (2017) 2693–2701.
- [52] W. Ma, N. Wang, Y. Fan, T. Tong, X. Han, Y. Du, Non-radical-dominated catalytic degradation of bisphenol A by ZIF-67 derived nitrogen-doped carbon nanotubes frameworks in the presence of peroxyxonosulfate, *Chem. Eng. J.* 336 (2018) 721–731.
- [53] United Nations, Globally Harmonized System of Classification and Labelling of Chemical (GHS), 4th ed., United Nations Publications, New York, 2011.
- [54] US EPA, Toxicity Estimation Software Tool, Available at: (2016) <https://www.epa.gov/chemical-research/toxicity-estimation-software-tool-test>.
- [55] J. Kang, X.G. Duan, C. Wang, H.Q. Sun, X.Y. Tan, M.O. Tade, S.B. Wang, Nitrogen-doped bamboo-like carbon nanotubes with Ni encapsulation for persulfate activation to remove emerging contaminants with excellent catalytic stability, *Chem. Eng. J.* 332 (2018) 398–408.